
Article:
Verhoosel, C.V., Remmers, J.J.C., Gutiérrez, M.A. et al. (1 more author) (2010) Computational homogenization for adhesive and cohesive failure in quasi-brittle solids. International Journal for Numerical Methods in Engineering, 83 (8-9). pp. 1155-1179. ISSN 0029-5981

https://doi.org/10.1002/nme.2854

INTERNATIONAL JOURNAL FOR NUMERICAL METHODS IN ENGINEERING
Int. J. Numer. Meth. Engng 2000; **00**:1–6 *Prepared using* nmeauth.cls *[Version: 2002/09/18 v2.02]*

Computational homogenisation for adhesive and cohesive failure in quasi-brittle solids

Clemens V. Verhoosel[1]*, Joris J. C. Remmers[1], Miguel A. Gutiérrez[2] and René de Borst[1]

[1] *Department of Mechanical Engineering, Eindhoven University of Technology, 5600 MB, Eindhoven, The Netherlands*
[2] *Faculty of Mechanical, Maritime and Materials Engineering, Delft University of Technology, Delft, The Netherlands*

SUMMARY

A computational multiscale framework is proposed that incorporates microstructural behaviour in a macroscale discrete fracture model. Homogenisation procedures are derived for both adhesive and cohesive failure on the macroscale and are implemented in an FE^2-setting. The most important feature of the homogenisation procedure is that it implicitly defines a traction-opening relation for the macroscale fracture model. The representativeness of the micro models is studied using a one-dimensional example, which shows that in the softening regime the proposed multiscale scheme behaves different from a bulk homogenisation scheme. These results are also observed in a numerical simulation for a micro model with a periodic microstructure. Numerical simulations further demonstrate the applicability of the method. Copyright © 2000 John Wiley & Sons, Ltd.

KEY WORDS: computational homogenisation, multiscale, fracture, finite elements, partition of unity method

1. INTRODUCTION

The operational use of many engineering structures is restricted by the occurrence of failure. Understanding failure mechanisms as well as their prediction is of the utmost importance for improving the designs of these structures. Over the past decades, numerical methods have been used extensively to study failure processes and are by now well developed. The gained insight in the behaviour of these engineering materials, has led to the design of novel materials with increasing complexity. For many of these materials, various length scales can be identified. For example, closer inspection of a composite plate can reveal the presence of a microstructure composed of fibres and epoxy. Where on the larger scale failure of such a plate appears as a discrete crack, various competing failure mechanisms (e.g. fibre-epoxy debonding, epoxy

*Correspondence to: c.v.verhoosel@tue.nl, Department of Mechanical Engineering, Eindhoven University of Technology, 5600 MB, Eindhoven, The Netherlands

failure, etc.) can be present on the microscale. In many cases, a correct description of the macroscale behaviour requires consideration of the microstructure, which leads to multiscale analyses.

Conceptually, the most straightforward approach to failure processes in materials with a complex microstructure is to model the microstructure explicitly. Such a full-resolution modelling of the microscale is, however, often impractical from a computational effort point of view. Fortunately, from an engineering point of view, it is often unnecessary to mimic the complete microstructure. In many cases it is sufficient to only retrieve the most important characteristics of the microscale to obtain an appropriate macroscale model. This restricted interest in the microscale behaviour offers the possibility for multiscale analyses, in which only part of the microscale complexity is carried over to the macroscale.

In a multiscale analysis, information is exchanged between different length scales e.g. by means of homogenisation techniques. The development of such techniques dates back to the works of Voigt [1] and Reuss [2] in which rules of mixtures are applied to achieve effective properties of multiphase materials. Many homogenisation methods in which the solution of a microstructural problem is determined to obtain effective material properties were proposed, and especially the pioneering work of Eshelby [3] is worth mentioning. In more recent years, these closed-form homogenisation techniques have been used to determine effective material properties and homogenised constitutive laws, based on the numerical solution of a microscale problem. This type of numerical homogenisation methods are generally referred to as unit cell methods and have proven their worth. A significant disadvantage of the unit cell methods is that assumptions regarding the form of macroscale constitutive behaviour are required, which makes the method less appropriate for many nonlinear problems.

Computational homogenisation [4] is nowadays recognised as a suitable technique to overcome the limitations of unit cell methods. The key feature of computational homogenisation is that they describe the macroscopic constitutive behaviour using finite element models (or any other discretisation technique) on the microscale, rather than via analytic constitutive laws. This approach implies that an additional finite element model is solved in all macroscopic integration points. Although it may be computationally expensive, computational homogenisation has been demonstrated to be capable of effectively capturing nonlinear microscale behaviour in macroscale analyses [5, 6, 7].

The focus of computational homogenisation has been on the homogenisation of bulk properties. Recently, computational homogenisation techniques have also been applied to determine constitutive relations for predefined interfaces [8, 9] as well as for cohesive cracks [10]. Variational multiscale methods are nowadays also used to simulate microstructural effects on cohesive cracks [11]. An alternative homogenisation scheme for modelling cohesive cracks in piezoelectric materials was proposed in [12]. This framework is now applied to the mechanical case, and is extended to the case of adhesive interface fracture. The key feature of the proposed averaging scheme is that it provides traction-opening relations governing the evolution of macroscopic cracks. In the case of a cohesive crack, the averaging relations are applied to a finite element model representing the bulk material in the vicinity of a crack. In the case of an adhesive crack, the employed microscale model represents the material in the adhesive layer. Since for both cases the obtained macroscopic traction-opening relations are only defined on macroscopic cracks, the proposed averaging scheme can be regarded as a homogenisation procedure applied along the macroscopic cracks. The implications of this strategy on the existence of a representative volume element are discussed in this work. This discussion

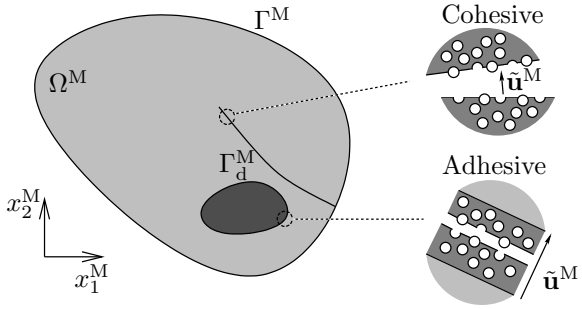

Figure 1. Schematic representation of the macroscale model. The internal boundary $\Gamma^{\mathrm{M}}_{\mathrm{d}}$ represents either a cohesive crack or an interfacial (or adhesive) crack.

will encompass a comparison with classical homogenisation schemes for softening media, for which RVEs are shown to be non-existent in the softening regime [13]. Some details on the numerical implementation of the developed FE^2-framework for adhesive and cohesive fracture are discussed.

After the introduction of the macroscale model in section 2 and the microscale model in section 3, the homogenisation framework for adhesive and cohesive failure is presented in section 4. Some relevant algorithmic aspects are then discussed in section 5. Numerical simulations are presented in section 6 that illustrate in what sense the microscale finite element models are representative for the macroscale behaviour of adhesive and cohesive cracks. The homogenisation techniques are further illustrated using two numerical examples with different macroscale discretisation techniques.

2. MACROSCALE MODEL

We consider the two-dimensional macroscale solid Ω^{M} with displacement field $\mathbf{u}^{\mathrm{M}}(\mathbf{x}^{\mathrm{M}})$ as shown in Figure 1. The superscript M is used to indicate that a variable is defined on the macroscale. A discontinuity in the displacement field $\tilde{\mathbf{u}}^{\mathrm{M}}$ occurs across the internal boundary $\Gamma^{\mathrm{M}}_{\mathrm{d}}$, representing either a cohesive crack or a predefined interface. In the case of a geometrically nonlinear kinematics description the internal boundary is defined as the centre line of the crack edges. These two types of fracture are illustrated schematically in Figure 1 and are referred to as cohesive and adhesive failure in the remainder of this work.

Quasi-static equilibrium of the body Ω^{M} is governed by

$$\begin{cases} \operatorname{div}\big(\boldsymbol{\sigma}^{\mathrm{M}}\big) = \mathbf{b}^{\mathrm{M}} & \mathbf{x}^{\mathrm{M}} \in \Omega^{\mathrm{M}} \\ \boldsymbol{\sigma}^{\mathrm{M}} \cdot \mathbf{n}^{\mathrm{M}} = \mathbf{t}^{\mathrm{M}}(\tilde{\mathbf{u}}^{\mathrm{M}}) & \mathbf{x}^{\mathrm{M}} \in \Gamma^{\mathrm{M}}_{\mathrm{d}} \\ \boldsymbol{\sigma}^{\mathrm{M}} \cdot \mathbf{n}^{\mathrm{M}} = \bar{\mathbf{t}}^{\mathrm{M}} & \mathbf{x}^{\mathrm{M}} \in \Gamma^{\mathrm{M}}_{\bar{t}} \\ \mathbf{u}^{\mathrm{M}} = \bar{\mathbf{u}}^{\mathrm{M}} & \mathbf{x}^{\mathrm{M}} \in \Gamma^{\mathrm{M}}_{\bar{u}} \end{cases} \tag{1}$$

with body forces $\mathbf{b}^{\mathrm{M}}$, boundary tractions $\bar{\mathbf{t}}^{\mathrm{M}}$ on $\Gamma^{\mathrm{M}}_{\bar{t}} \subseteq \Gamma^{\mathrm{M}}$ and boundary displacements $\bar{\mathbf{u}}^{\mathrm{M}}$ on $\Gamma^{\mathrm{M}}_{\bar{u}} \subseteq \Gamma^{\mathrm{M}}$. The tractions are related to the Cauchy stresses by the normal vectors $\mathbf{n}^{\mathrm{M}}$ (with corresponding orthogonal shear vectors $\mathbf{s}^{\mathrm{M}}$). Solving these equations requires setting

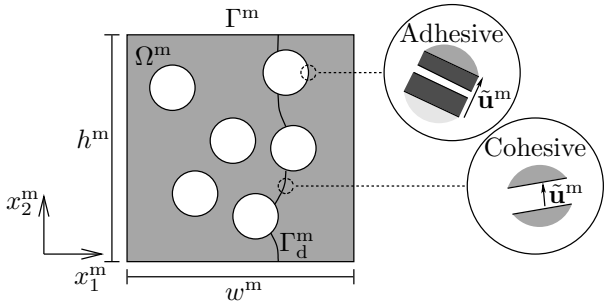

Figure 2. Schematic representation of the microscale model. Both initially elastic interfacial (or adhesive) cracks and initially rigid cohesive cracks can occur.

up constitutive relations for the Cauchy stress $\boldsymbol{\sigma}^{\mathrm{M}}$ and corresponding traction $\mathbf{t}^{\mathrm{M}}$. These complementary relations are here provided by means of the homogenisation methods discussed in section 4.

The constitutive homogenisation framework proposed in this paper is independent of the considered macroscale formulation for discrete crack modelling. The two most commonly used approaches for modelling quasi-brittle failure are the use of interface elements [14] and, more recently, the partition of unity-based methods [15, 16, 17]. Some details on the employed macroscale models will be provided in the numerical simulations section. Both formulations are based on the finite element method, which discretises the displacement field using the nodal displacement vector $\mathbf{a}^{\mathrm{M}}$. The quasi-static equilibrium of the solid is then given by

$$\mathbf{f}_{\mathrm{int}}^{\mathrm{M}}(\mathbf{a}^{\mathrm{M}}) = \mathbf{f}_{\mathrm{ext}}^{\mathrm{M}} \tag{2}$$

with $\mathbf{f}_{\mathrm{int}}^{\mathrm{M}}$ and $\mathbf{f}_{\mathrm{ext}}^{\mathrm{M}}$ being the macroscopic internal and external force vector, respectively. The internal force vector is related to the Cauchy stress $\boldsymbol{\sigma}^{\mathrm{M}}$ in the bulk material and traction $\mathbf{t}^{\mathrm{M}}$ on the discontinuity surface by

$$\mathbf{f}_{\mathrm{int}}^{\mathrm{M}} = \mathbf{f}_{\mathrm{int}}^{\mathrm{M}}\left(\boldsymbol{\sigma}^{\mathrm{M}}, \mathbf{t}^{\mathrm{M}}\right) \tag{3}$$

Similarly, the external force vector can be related to the body forces $\mathbf{b}^{\mathrm{M}}$ and traction $\bar{\mathbf{t}}^{\mathrm{M}}$. The prescribed boundary displacements $\bar{\mathbf{u}}^{\mathrm{M}}$ are generally applied by means of constraints of the equation solver.

3. MICROSCALE MODEL

Consistent with the employed macroscale formulations, failure models with a localised damage zone are considered on the microscale. Basically, this means that the micro models need to display softening behaviour. For such micro models the definition of representative volume elements has been demonstrated to be troublesome when using a classical homogenisation approach [13]. A discussion on the representativeness of the micro models in the context of the homogenisation framework proposed in this work is presented in section 6.1. Here, the homogenisation framework is derived for the case that the fracture process on the microscale is described by a discrete fracture model, but could also be applied to the case of smeared models, such as gradient-enhanced continuum damage [18].

The two-dimensional model as shown in Figure 2 is studied on the microscale. The microscale domain Ω^{m} is rectangular with dimensions $w^{\mathrm{m}} \times h^{\mathrm{m}}$, where use is made of the superscript m to indicate that a microscale quantity is concerned. Although the geometry of the microscale model is regular, the composition of the material is generally complex. On the microscale, displacements and displacement gradients are assumed to be small, thereby permitting the use of a linear kinematics description. Discrete jumps in the displacement field $\tilde{\mathbf{u}}^{\mathrm{m}}$ are assumed across the internal boundary $\Gamma_{\mathrm{d}}^{\mathrm{m}}$. As schematically shown in Figure 2, both adhesive and cohesive failure processes are considered on the microscale. Therefore the internal boundary $\Gamma_{\mathrm{d}}^{\mathrm{m}}$ is comprised of the cracks running through the bulk material and the interfacial delaminations of the various material interfaces.

The quasi-static equilibrium of the microscale model is described by

$$\begin{cases} \operatorname{div}(\boldsymbol{\sigma}^{\mathrm{m}}) = \mathbf{b}^{\mathrm{m}} & \mathbf{x}^{\mathrm{m}} \in \Omega^{\mathrm{m}} \\ \boldsymbol{\sigma}^{\mathrm{m}} \cdot \mathbf{n}^{\mathrm{m}} = \mathbf{t}^{\mathrm{m}}(\tilde{\mathbf{u}}^{\mathrm{m}}) & \mathbf{x}^{\mathrm{m}} \in \Gamma_{\mathrm{d}}^{\mathrm{m}} \\ \mathbf{u}^{\mathrm{m}} = \bar{\mathbf{u}}^{\mathrm{m}} & \mathbf{x}^{\mathrm{m}} \in \Gamma_{\bar{u}}^{\mathrm{m}} \end{cases} \tag{4}$$

Although these expressions closely resemble the macroscale equilibrium equations, the microscale model is fundamentally different since the constitutive relations for the microscale Cauchy stress $\boldsymbol{\sigma}^{\mathrm{m}}$ and microscale traction $\mathbf{t}^{\mathrm{m}}$ are described using analytical expressions. In addition, the traction boundary conditions are omitted in equation (4). The reason for this is that in the multiscale framework, only displacement boundary conditions (including periodic displacement conditions) are used.

In this contribution, both adhesive and cohesive microscale cracks are modelled using interface elements. Initially elastic interface elements are used for the adhesive cracks and initially rigid interfaces for the cohesive cracks. Some details on the microscale model implementation are provided in the section on the numerical simulations. It is emphasised that other discretisation techniques, such as the partition of unity method, could be used equally well to model discontinuities on the microscale.

In the case that a finite element discretisation is employed for the microscale displacement field, the equilibrium of the microscale can be represented by the system of equations

$$\mathbf{f}_{\mathrm{int}}^{\mathrm{m}}(\mathbf{a}^{\mathrm{m}}) = \mathbf{f}_{\mathrm{ext}}^{\mathrm{m}} \tag{5}$$

with $\mathbf{a}^{\mathrm{m}}$, $\mathbf{f}_{\mathrm{int}}^{\mathrm{m}}$ and $\mathbf{f}_{\mathrm{ext}}^{\mathrm{m}}$ being the microscale nodal displacement vector, internal force vector and external force vector, respectively.

4. CONSTITUTIVE HOMOGENISATION

In the case of adhesive failure, averaging relations are derived to relate the macroscale traction-opening law to the response of the microscale model. In the case that failure of an adhesive layer is studied, the constitutive behaviour of the macroscale bulk material is obviously not related to that of the microscale model.

For a proper description of a multiscale constitutive model for cohesive failure it is of crucial importance to note that the failure description can be fundamentally different on the two scales. On the macroscale, a cohesive zone is only inserted upon satisfaction of a failure criterion, assuming the material behaves linearly until crack nucleation. In contrast, the moment of

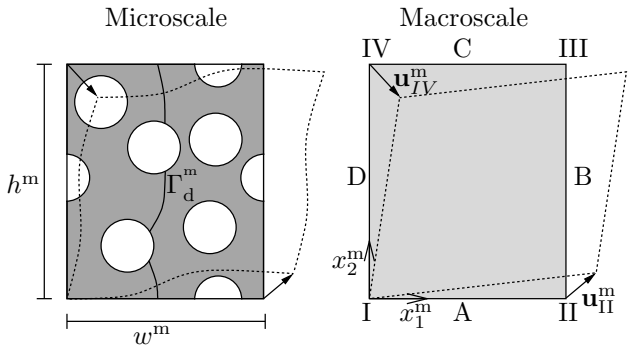

Figure 3. Schematic representation of the micro model used for the homogenisation of the bulk material properties.

failure on the microscale is not well defined, since on this scale damage more gradually degrades the material. In the present framework, it is assumed that the macroscale constitutive behaviour prior to the insertion of a cohesive segment can be described on the basis of the homogenised microscale properties in the undeformed state. Therefore, the nonlinear behaviour of the microscale model prior to macroscale fracture is not incorporated in the formulation. This neglect of nonlinear behaviour prior to softening is consistent with the assumptions made on the macroscale.

4.1. Bulk constitutive behaviour

The bulk constitutive behaviour is described by the microscale model schematically shown in Figure 3. For notational convenience a single discontinuity $\Gamma^{\mathrm{m}}_{\mathrm{d}}$ is considered that splits the microstructure into two parts. The derivation, however, remains fully valid for multiple discontinuities. In case of a single discontinuity, the microscale displacement field can be decomposed as

$$\mathbf{u}^{\mathrm{m}} = \langle \boldsymbol{\varepsilon}^{\mathrm{m}} \rangle_{\Omega^{\mathrm{m}}} \cdot \mathbf{x}^{\mathrm{m}} + \underbrace{\bar{\mathbf{u}}^{\mathrm{m}} + \mathcal{H}_{\Gamma^{\mathrm{m}}_{\mathrm{d}}} \tilde{\mathbf{u}}^{\mathrm{m}}}_{\check{\mathbf{u}}^{\mathrm{m}}} \tag{6}$$

with $\mathcal{H}_{\Gamma^{\mathrm{m}}_{\mathrm{d}}}$ being equal to 1 on one side of the discontinuity and 0 one the other side. The boundary conditions for the micro model are then given in terms of the microscopic fluctuation fields $\check{\mathbf{u}}^{\mathrm{m}}$. On the four control nodes (I to IV), the displacement fluctuations are equal to zero. Moreover, the fluctuation field is periodic from the left to the right edge and from the bottom to the top edge (as indicated by the dotted lines in Figure 3). Note that the geometry of the microscale model is assumed to be periodic as well. From these boundary conditions, it follows that the homogenised engineering strain $\langle \boldsymbol{\varepsilon}^{\mathrm{m}} \rangle_{\Omega^{\mathrm{m}}}$ is defined as the volume average of the corresponding microscopic fields

$$\langle \boldsymbol{\varepsilon}^{\mathrm{m}} \rangle_{\Omega^{\mathrm{m}}} = \frac{1}{w^{\mathrm{m}} h^{\mathrm{m}}} \int_{\Omega^{\mathrm{m}}} \boldsymbol{\varepsilon}^{\mathrm{m}} \mathrm{d}\Omega^{\mathrm{m}} = \frac{1}{w^{\mathrm{m}}} \mathbf{a}^{\mathrm{m}}_{\mathrm{II}} \otimes^{\mathrm{s}} \mathbf{n}^{\mathrm{M}} + \frac{1}{h^{\mathrm{m}}} \mathbf{a}^{\mathrm{m}}_{\mathrm{IV}} \otimes^{\mathrm{s}} \mathbf{s}^{\mathrm{M}} \tag{7}$$

where $\mathbf{a}^{\mathrm{M}}_{\mathrm{II}}$ and $\mathbf{a}^{\mathrm{M}}_{\mathrm{IV}}$ are the displacements of the finite element nodes at point II and IV, respectively, and $\square \otimes^{\mathrm{s}} \square = \mathrm{sym}(\square \otimes \square)$ is the symmetrised dyadic product. In this expression, the divergence theorem is used to rewrite the volume integral as a boundary integral. Using

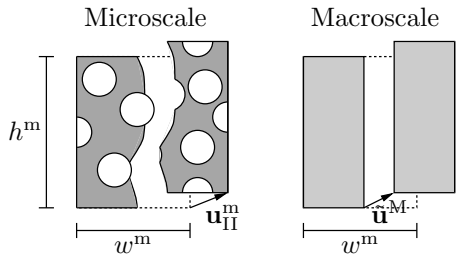

Figure 4. Schematic representation of homogenisation schemes for cohesive failure.

the periodicity of the fluctuation field, the homogenised strain can be written in terms of the nodal displacements corresponding to the control nodes. Please note that the opening of the discontinuity $\Gamma^{\mathrm{m}}_{\mathrm{d}}$ can contribute to this homogenised strain.

The definition of the homogenised stress follows by consideration of the Hill-Mandel energy condition [19]

$$\langle \boldsymbol{\sigma}^{\mathrm{m}} \rangle_{\Omega^{\mathrm{m}}} : \delta \langle \boldsymbol{\varepsilon}^{\mathrm{m}} \rangle_{\Omega^{\mathrm{m}}} = \frac{1}{w^{\mathrm{m}} h^{\mathrm{m}}} \int_{\Omega^{\mathrm{m}}} \boldsymbol{\sigma}^{\mathrm{m}} : \delta \boldsymbol{\varepsilon}^{\mathrm{m}} \mathrm{d}\Omega^{\mathrm{m}} = \frac{1}{w^{\mathrm{m}} h^{\mathrm{m}}} \int_{\Gamma^{\mathrm{m}}} \mathbf{t}^{\mathrm{m}} \otimes \mathbf{x}^{\mathrm{m}} \mathrm{d}\Gamma^{\mathrm{m}} : \delta \langle \boldsymbol{\varepsilon} \rangle_{\Omega^{\mathrm{m}}} \tag{8}$$

where use has been made of equilibrium at the microscale to rewrite the volume integral as a boundary integral. In addition, use has been made of the anti-periodicity of the traction corresponding to the periodic boundary conditions for the displacements. Using the divergence theorem, the homogenised stress is obtained as

$$\langle \boldsymbol{\sigma}^{\mathrm{m}} \rangle_{\Omega^{\mathrm{m}}} = \frac{1}{w^{\mathrm{m}} h^{\mathrm{m}}} \int_{\Omega^{\mathrm{m}}} \boldsymbol{\sigma}^{\mathrm{m}} \mathrm{d}\Omega^{\mathrm{m}} = \frac{1}{h^{\mathrm{m}}} \mathbf{f}^{\mathrm{m}}_{\mathrm{B}} \otimes \mathbf{n}^{\mathrm{M}} + \frac{1}{w^{\mathrm{m}}} \mathbf{f}^{\mathrm{m}}_{\mathrm{C}} \otimes \mathbf{s}^{\mathrm{M}} \tag{9}$$

Hence, the homogenised kinetic properties are the volume averages of the microscopic quantities, when use is made of the boundary conditions specified. We note that the homogenised stress tensor is symmetric by virtue of the equilibrium of moments. In terms of the microscale finite element force vector, this expression is determined on the basis of only the values of the internal force vectors in the nodes on the right (B) and top (C) boundary.

The macroscopic Cauchy stress is related to the macroscopic engineering strain using the homogenised material tangent in the undeformed state as

$$\boldsymbol{\sigma}^{\mathrm{M}} = \underbrace{\left. \frac{\partial \langle \boldsymbol{\sigma}^{\mathrm{m}} \rangle_{\Omega^{\mathrm{m}}}}{\partial \langle \boldsymbol{\varepsilon}^{\mathrm{m}} \rangle_{\Omega^{\mathrm{m}}}} \right|_{\mathbf{u}^{\mathrm{m}}=\mathbf{0}}}_{\mathbf{H}} : \boldsymbol{\varepsilon}^{\mathrm{M}} \tag{10}$$

The consistent tangent in the undeformed state $\mathbf{H}_0$ is obtained by using the equations (7) and (9) in combination with condensation of the microscopic tangent matrix in the undeformed state [20]. During the macroscopic finite element simulation, the bulk stresses are computed by the evaluation of the analytical expression (10).

4.2. Cohesive interface constitutive behaviour

To derive a homogenisation scheme for the macroscopic traction-opening relation for a cohesive crack, the microscale model shown in Figure 4 is considered. From Figure 4 it is apparent

that the averaged micro model is homogeneous in the direction along the crack, but not in the direction perpendicular to it. For that reason the proposed multiscale framework is not a homogenisation method in the literal sense of the word. Instead, when we refer to the proposed method as a homogenisation technique we refer to the fact that the method couples a micro- and macroscale.

In the absence of an obvious definition for the homogenised crack opening $\tilde{\mathbf{u}}^{\mathrm{M}}$, the homogenised (or macroscopic) traction $\mathbf{t}^{\mathrm{M}}$ is postulated as the projection of the macroscopic Cauchy stress on the macroscopic crack plane, yielding

$$\mathbf{t}^{\mathrm{M}} = \boldsymbol{\sigma}^{\mathrm{M}} \cdot \mathbf{n}^{\mathrm{M}} = \frac{1}{h^{\mathrm{m}}} \mathbf{f}^{\mathrm{m}}_{\mathrm{B}} \tag{11}$$

where equation (9) is used to express the macroscopic traction in terms of the microscopic finite element force vectors. Note that both the microscale material tangents and microscale geometry need to be considered in the microscale reference frame. In this work, microscale isotropy is assumed to make these consideration unnecessary.

The corresponding homogenisation law for the macroscopic crack opening is then obtained using the Hill-Mandel energy condition. In the case of a cohesive crack, this condition reads

$$\boldsymbol{\sigma}^{\mathrm{M}} : \delta\boldsymbol{\varepsilon}^{\mathrm{M}} + \frac{1}{w^{\mathrm{m}}} \mathbf{t}^{\mathrm{M}} \cdot \delta\tilde{\mathbf{u}}^{\mathrm{M}} = \frac{1}{w^{\mathrm{m}} h^{\mathrm{m}}} \int_{\Gamma^{\mathrm{m}}} \mathbf{t}^{\mathrm{m}} \cdot \delta\mathbf{u}^{\mathrm{m}} \mathrm{d}\Gamma^{\mathrm{m}} \tag{12}$$

as schematically illustrated in Figure 4. As can be seen, this expression is composed of a part concerning the internal work of the bulk material and a part representing the work performed by the cohesive surface. Using the microscale boundary conditions, the boundary integral in equation (12) is rewritten to yield

$$\boldsymbol{\sigma}^{\mathrm{M}} : \delta\boldsymbol{\varepsilon}^{\mathrm{M}} + \frac{1}{w^{\mathrm{m}}} \mathbf{t}^{\mathrm{M}} \cdot \delta\tilde{\mathbf{u}}^{\mathrm{M}} = \frac{1}{w^{\mathrm{m}}} \mathbf{t}^{\mathrm{M}} \cdot \delta\mathbf{u}^{\mathrm{m}}_{\mathrm{II}} \tag{13}$$

with $\mathbf{u}^{\mathrm{m}}_{\mathrm{II}}$ being the displacement of the bottom right control node (node II). For the used boundary conditions, the macroscopic stress as given in (9) can be written as

$$\boldsymbol{\sigma}^{\mathrm{M}} = \frac{1}{h^{\mathrm{m}}}^{\mathrm{M}} \int_{\Gamma^{\mathrm{m}}_{\mathrm{B}}} \mathbf{t}^{\mathrm{m}} \mathrm{d}\Gamma^{\mathrm{m}}_{\mathrm{B}} \otimes \mathbf{n} + \frac{1}{w^{\mathrm{m}}} \int_{\Gamma^{\mathrm{m}}_{\mathrm{C}}} \mathbf{t}^{\mathrm{m}} \mathrm{d}\Gamma^{\mathrm{m}}_{\mathrm{C}} \otimes \mathbf{s} = \boldsymbol{\Delta} \cdot \mathbf{t}^{\mathrm{M}} \tag{14}$$

with the third-order tensor $\boldsymbol{\Delta} = \mathbf{n}\otimes\mathbf{n}\otimes\mathbf{n} + (\mathbf{n}\otimes\mathbf{s} + \mathbf{s}\otimes\mathbf{n})\otimes\mathbf{s}$. Using this expression, equation (13) can be reformulated as

$$\mathbf{t}^{\mathrm{M}} \cdot \left(\underbrace{\left[\boldsymbol{\Delta}^{\overset{13}{\mathrm{T}}} \cdot \mathbf{H}^{-1} \cdot \boldsymbol{\Delta} \right]}_{\mathbf{C}} \cdot \delta\mathbf{t}^{\mathrm{M}} + \frac{1}{w^{\mathrm{m}}} \delta\tilde{\mathbf{u}}^{\mathrm{M}} \right) = \mathbf{t}^{\mathrm{M}} \cdot \left(\frac{1}{w^{\mathrm{m}}} \delta\mathbf{u}^{\mathrm{m}}_{\mathrm{II}} \right) \tag{15}$$

where $\square^{\overset{13}{\mathrm{T}}}$ swaps the first and third index in a third order tensor ($\square^{\overset{13}{\mathrm{T}}}_{ijk} = \square_{kji}$) and use has been made of the symmetries of the fourth-order compliance tensor $\mathbf{H}^{-1}$. Note that the second-order tensor $\mathbf{C}$ is a projection on the crack plane of the fourth-order compliance tensor.

Since equation (15) should hold for any value of the macroscopic traction, it follows that

$$\mathbf{C} \cdot \delta\mathbf{t}^{\mathrm{M}} + \frac{1}{w^{\mathrm{m}}} \delta\tilde{\mathbf{u}}^{\mathrm{M}} = \frac{1}{w^{\mathrm{m}}} \delta\mathbf{u}^{\mathrm{m}}_{\mathrm{II}} \tag{16}$$

This equation can be rewritten as

$$\delta \mathbf{u}_{\mathrm{II}}^{\mathrm{m}} = w^{\mathrm{m}} \mathbf{C}_0 \cdot \delta \mathbf{t}^{\mathrm{M}} + \delta \mathring{\mathbf{u}}^{\mathrm{M}} + \delta \tilde{\mathbf{u}}^{\mathrm{M}} \tag{17}$$

with $\mathbf{C}_0$ being the projection on the discontinuity plane of the compliance tensor $\mathbf{H}_0$ in the undeformed state, and $\mathring{\mathbf{u}}^{\mathrm{M}}$ a compatibility displacement for which

$$\delta \mathring{\mathbf{u}}^{\mathrm{M}} = w^{\mathrm{m}} \left[\mathbf{C} - \mathbf{C}_0 \right] \delta \mathbf{t}^{\mathrm{M}} \tag{18}$$

In this contribution it is assumed that after macroscopic crack nucleation, i.e. the part where the cohesive homogenisation scheme is used, the nonlinearity in $\mathbf{u}_{\mathrm{II}}^{\mathrm{m}}$ is completely caused by the macroscopic displacement jump $\tilde{\mathbf{u}}^{\mathrm{M}}$. Then $\delta \mathring{\mathbf{u}}^{\mathrm{M}}$ is equal to zero, yielding

$$\mathbf{u}_{\mathrm{II}}^{\mathrm{m}} = w^{\mathrm{m}} \mathbf{C}_0 \cdot \mathbf{t}^{\mathrm{M}} + \mathring{\mathbf{u}}^{\mathrm{M}} + \tilde{\mathbf{u}}^{\mathrm{M}} \tag{19}$$

In this expression $\mathring{\mathbf{u}}^{\mathrm{M}}$ is computed at nucleation, i.e. when $\tilde{\mathbf{u}}^{\mathrm{M}} = \mathbf{0}$. Since the macroscopic traction $\mathbf{t}^{\mathrm{M}}$ is a nonlinear function of the microscopic displacement $\mathbf{u}_{\mathrm{II}}^{\mathrm{m}}$, equation (19) is a set of nonlinear equations that can be solved for a given macroscopic crack opening $\tilde{\mathbf{u}}^{\mathrm{M}}$. Therefore, equation (19) serves as a constitutive law for the cohesive interfaces. This constitutive law also provides a physical interpretation. The macroscopic crack opening ($\tilde{\mathbf{u}}^{\mathrm{M}}$) is defined as the average displacement over the right edge of the specimen ($\mathbf{u}_{\mathrm{II}}^{\mathrm{m}}$) minus the elastic displacement of that edge ($w^{\mathrm{m}} \mathbf{C}_0 \cdot \mathbf{t}^{\mathrm{M}}$). The compatibility displacement ($\mathring{\mathbf{u}}^{\mathrm{M}}$) is merely a numerical parameter to connect the pre-failure part of the response to the post-failure part. In summary, the crack opening is defined as the non-elastic part of the average displacement difference between the right and left edge of the micro model.

In terms of the microscale finite element displacement vector, the cohesive law (19) can be written as

$$\mathbf{M}^{\mathrm{T}} \mathbf{a}^{\mathrm{m}} = w^{\mathrm{m}} \mathbf{C}_0 \mathbf{t}^{\mathrm{M}} + \mathring{\mathbf{u}}^{\mathrm{M}} + \tilde{\mathbf{u}}^{\mathrm{M}} \tag{20}$$

with $\mathbf{u}_{\mathrm{II}}^{\mathrm{m}} = \mathbf{a}_{\mathrm{II}}^{\mathrm{m}} = \mathbf{M}^{\mathrm{T}} \mathbf{a}^{\mathrm{m}}$. Note that in this expression, matrix-vector notation is used instead of tensor notation. In combination with equation (11), this equation yields the nonlinear system of equations that governs microscale equilibrium

$$\begin{pmatrix} \mathbf{f}_{\mathrm{int}}^{\mathrm{m}} - h^{\mathrm{m}} \mathbf{M} \mathbf{t}^{\mathrm{M}} \\ \mathbf{M}^{\mathrm{T}} \mathbf{a}^{\mathrm{m}} - w^{\mathrm{m}} \mathbf{C}_0 \mathbf{t}^{\mathrm{M}} \end{pmatrix} = \begin{pmatrix} \mathbf{0} \\ \mathring{\mathbf{u}}^{\mathrm{M}} + \tilde{\mathbf{u}}^{\mathrm{M}} \end{pmatrix} \tag{21}$$

which can, given a specified macroscopic opening $\tilde{\mathbf{u}}^{\mathrm{M}}$, be solved incrementally for $\mathbf{a}^{\mathrm{m}}$ and $\mathbf{t}^{\mathrm{M}}$ using

$$\begin{bmatrix} \mathbf{K}^{\mathrm{m}} & -h^{\mathrm{m}} \mathbf{M} \\ \mathbf{M}^{\mathrm{T}} & -w^{\mathrm{m}} \mathbf{C}_0 \end{bmatrix} \begin{pmatrix} \delta \mathbf{a}^{\mathrm{m}} \\ \delta \mathbf{t}^{\mathrm{M}} \end{pmatrix} = \begin{pmatrix} \mathbf{0} \\ \delta \tilde{\mathbf{u}}^{\mathrm{M}} \end{pmatrix} \tag{22}$$

This system of equations can easily be made symmetric by e.g. multiplying the second row of equation with $-h^{\mathrm{m}}$. The reason that a symmetric system can be found is that the system of equations results from the minimisation of the functional

$$\Pi \left(\mathbf{a}^{\mathrm{m}}, \mathbf{t}^{\mathrm{M}} \right) = \Pi^{\mathrm{m}} \left(\mathbf{a}^{\mathrm{m}} \right) + \Pi^{\mathrm{M}} \left(\mathbf{a}^{\mathrm{m}}, \mathbf{t}^{\mathrm{M}} \right) \tag{23}$$

with

$$\Pi^{\mathrm{m}} \left(\mathbf{a}^{\mathrm{m}} \right) = \int_{\Omega^{\mathrm{m}}} W_{\boldsymbol{\sigma}}^{\mathrm{m}} (\boldsymbol{\varepsilon}^{\mathrm{m}} \left(\mathbf{a}^{\mathrm{m}} \right)) \mathrm{d}\Omega^{\mathrm{m}} + \int_{\Gamma_{\mathrm{d}}^{\mathrm{m}}} W_{\mathbf{t}}^{\mathrm{m}} (\tilde{\mathbf{u}}^{\mathrm{m}} \left(\mathbf{a}^{\mathrm{m}} \right)) \mathrm{d}\Gamma_{\mathrm{d}}^{\mathrm{m}} \tag{24}$$

$$\Pi^{\mathrm{M}} \left(\mathbf{a}^{\mathrm{m}}, \mathbf{t}^{\mathrm{M}} \right) = \frac{1}{2} w^{\mathrm{m}} h^{\mathrm{m}} \left(\mathbf{C}_0 \mathbf{t}^{\mathrm{M}} \right)^{\mathrm{T}} \mathbf{t}^{\mathrm{M}} + h^{\mathrm{m}} \left(\mathring{\mathbf{u}}^{\mathrm{M}} + \tilde{\mathbf{u}}^{\mathrm{M}} - \mathbf{u}_{\mathrm{II}}^{\mathrm{m}} \left(\mathbf{a}^{\mathrm{m}} \right) \right)^{\mathrm{T}} \mathbf{t}^{\mathrm{M}} \tag{25}$$

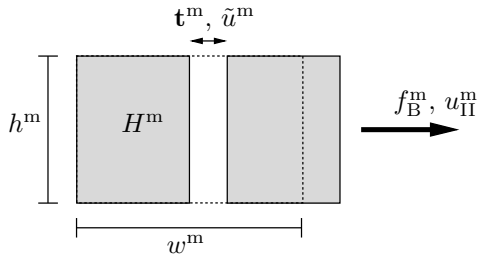

Figure 5. One-dimensional example of a microscale model. The microscale domain $w^{\mathrm{m}} \times h^{\mathrm{m}}$ with modulus of elasticity H^{m} is split into two parts by a cohesive interface with traction-opening law $t^{\mathrm{m}} = t^{\mathrm{m}}(\tilde{u}^{\mathrm{m}})$. In addition, $u_{\mathrm{II}}^{\mathrm{m}}$ and f_B^{m} are the displcement of the right edge and total reaction force over that edge, respectively.

In these expressions $W_{\boldsymbol{\sigma}}^{\mathrm{m}}$ and $W_{\mathbf{t}}^{\mathrm{m}}$ are defined such that

$$\boldsymbol{\sigma}^{\mathrm{m}} = \frac{\partial W_{\boldsymbol{\sigma}}^{\mathrm{m}}}{\partial \boldsymbol{\varepsilon}^{\mathrm{m}}} \qquad \text{and} \qquad \mathbf{t}^{\mathrm{m}} = \frac{\partial W_{\mathbf{t}}^{\mathrm{m}}}{\partial \tilde{\mathbf{u}}^{\mathrm{m}}} \tag{26}$$

The first functional (24) we recognise as the potential energy of the microscale model, whereas the second functional (25) requires the homogenised crack opening ($\tilde{\mathbf{u}}^{\mathrm{M}}$) to be equal to the total micro model displacement minus the elastic displacement ($\mathbf{u}_{\mathrm{II}}^{\mathrm{m}} - \mathring{\mathbf{u}}^{\mathrm{M}} - \mathbf{C}_0\mathbf{t}^{\mathrm{M}}$).

The augmented system of equations (22) can be solved efficiently using block-matrix inversion, which preserves the sparsity of the microscale consistent tangent $\mathbf{K}^{\mathrm{m}}$. After the cohesive interface has been inserted, $\delta\mathring{\mathbf{u}}^{\mathrm{M}}$ is assumed to be equal to zero. Equation (22) can also be rewritten to obtain the macroscopic material tangent

$$\frac{\partial \mathbf{t}^{\mathrm{M}}}{\partial \tilde{\mathbf{u}}^{\mathrm{M}}} = \left[h^{\mathrm{m}} \mathbf{M}^{\mathrm{T}} \left[\mathbf{K}^{\mathrm{m}}\right]^{-1} \mathbf{M} - w^{\mathrm{m}} \mathbf{C}_0 \right]^{-1} = \mathbf{S}^{-1} \tag{27}$$

Since the term $\left[\mathbf{K}^{\mathrm{m}}\right]^{-1}\mathbf{M}$ is already required for the solution of (22), this material tangent can be computed with negligible additional computational effort.

Numerical difficulties in the solution procedure are encountered when the determinant D of the matrix $\mathbf{S}$ equals to zero. In order to show the restrictions of the homogenisation scheme, we consider the one-dimensional example shown in Figure 5, for which the determinant D is determined as

$$D = \frac{h^{\mathrm{m}}}{K^{\mathrm{m}}} - w^{\mathrm{m}} C_0 = \frac{\frac{\mathrm{d}t^{\mathrm{m}}}{\mathrm{d}\tilde{u}^{\mathrm{m}}}\Big|_{\tilde{u}^{\mathrm{m}}=0} - \frac{\mathrm{d}t^{\mathrm{m}}}{\mathrm{d}\tilde{u}^{\mathrm{m}}}}{\frac{\mathrm{d}t^{\mathrm{m}}}{\mathrm{d}\tilde{u}^{\mathrm{m}}} \frac{\mathrm{d}t^{\mathrm{m}}}{\mathrm{d}\tilde{u}^{\mathrm{m}}}\Big|_{\tilde{u}^{\mathrm{m}}=0}} \tag{28}$$

From this result it is apparent that numerical instabilities will occur when the derivative of the microscopic traction with respect to the microscopic opening equals its value in the undeformed state. For damage models (with secant unloading) this is usually only the case in the absence of damage. Therefore these numerical instabilities can be circumvented by only using the homogenisation law after some damage has accumulated in the micro model. As outlined in the introduction of this section, this is generally the case and therefore no numerical difficulties have been encountered in the numerical simulations considered in section 6.

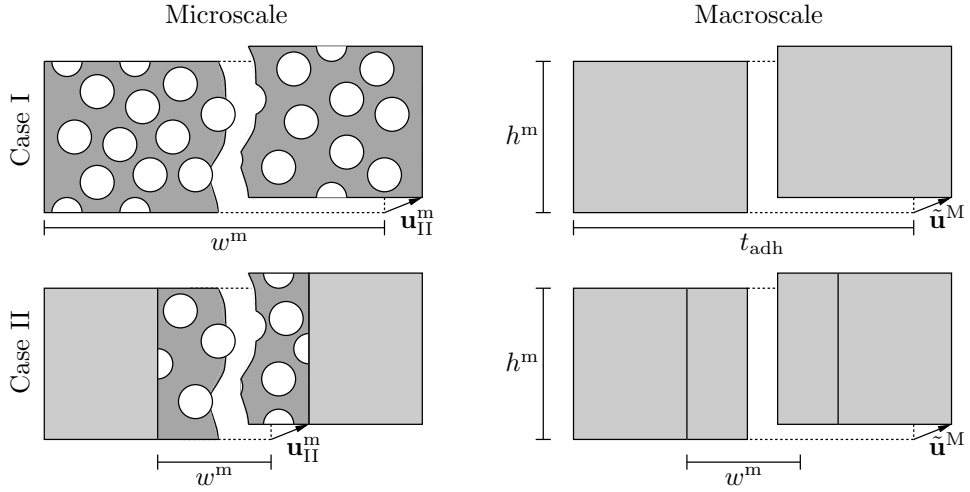

Figure 6. Schematic representation of homogenisation schemes for adhesive failure. For the Case I homogenisation scheme, the complete interface thickness is considered as a microscale model. For the Case II scheme, periodicity of the microstructure in the thickness direction is presumed.

4.3. Adhesive interface constitutive behaviour

For the homogenisation of an adhesive constitutive law, two types of micro models are considered, as illustrated in Figure 6. In the first case, the microscale model covers the complete thickness of the adhesive interface. This case is closely related to the multiscale models presented in Refs. [8, 21] and bears similarities with the coupled volume model introduced in Ref. [22]. In the second case, the interface behaviour is determined based on the behaviour of the material inside the adhesive layer in the vicinity of the crack. This case is more closely related to the multiscale procedure for cohesive fracture introduced in the previous section. Remind that as both averaged micro models are not homogeneous in the direction perpendicular to the crack, the derived averaging procedure should be regarded as homogenisation applied along the adhesive interface.

4.3.1. Case I In the case that the complete thickness of the adhesive interface is modelled by the micromodel, the macroscopic crack opening $\tilde{\mathbf{u}}^{\mathrm{M}}$ can be related directly to the displacement of the microscale $\mathbf{u}^{\mathrm{m}}_{\mathrm{II}}$ using

$$\tilde{\mathbf{u}}^{\mathrm{M}} = \mathbf{u}^{\mathrm{m}}_{\mathrm{II}} = \mathbf{a}^{\mathrm{m}}_{\mathrm{II}} \tag{29}$$

For this kind of micro model, the microscopic fluctuation field is assumed to be equal to zero on the left and right edge, and periodic from the top to the bottom edge.

The Hill-Mandel energy condition reads for this case

$$\frac{1}{w^{\mathrm{m}}}\mathbf{t}^{\mathrm{M}} \cdot \delta\tilde{\mathbf{u}}^{\mathrm{M}} = \frac{1}{w^{\mathrm{m}}h^{\mathrm{m}}}\int_{\Gamma^{\mathrm{m}}} \mathbf{t}^{\mathrm{m}} \cdot \delta\mathbf{u}^{\mathrm{m}} \mathrm{d}\Gamma^{\mathrm{m}} = \frac{1}{w^{\mathrm{m}}h^{\mathrm{m}}}\int_{\Gamma^{\mathrm{m}}} \mathbf{t}^{\mathrm{m}} \mathrm{d}\Gamma^{\mathrm{m}} \cdot \delta\mathbf{u}^{\mathrm{m}}_{\mathrm{II}} \tag{30}$$

so that the macroscopic traction

$$\mathbf{t}^{\mathrm{M}} = \frac{1}{h^{\mathrm{m}}}\int_{\Gamma^{\mathrm{m}}} \mathbf{t}^{\mathrm{m}} \mathrm{d}\Gamma^{\mathrm{m}} = \frac{1}{h^{\mathrm{m}}}\mathbf{f}_{\mathrm{B}} \tag{31}$$

resembles the expression (11) found for the cohesive interface.

Following the derivations in the previous section, the macroscopic traction $\mathbf{t}^{\mathrm{M}}$ can be obtained by solving the nonlinear system of equations

$$\begin{pmatrix} \mathbf{f}_{\mathrm{int}}^{\mathrm{m}} - h^{\mathrm{m}}\mathbf{M}\mathbf{t}^{\mathrm{M}} \\ \mathbf{M}^{\mathrm{T}}\mathbf{a}^{\mathrm{m}} \end{pmatrix} = \begin{pmatrix} \mathbf{0} \\ \tilde{\mathbf{u}}^{\mathrm{M}} \end{pmatrix} \tag{32}$$

for a given macroscopic crack opening $\tilde{\mathbf{u}}^{\mathrm{M}}$. Since the adhesive interfaces are inserted in the undeformed state, the compatibility displacement $\mathring{\mathbf{u}}^{\mathrm{M}}$ is equal to zero.

For the one-dimensional example shown in Figure 5, the determinant of matrix $\mathbf{S}$, as introduced in equation (27), corresponding to the system (32) is given by

$$D = \frac{h^{\mathrm{m}}}{K^{\mathrm{m}}} = \frac{H^{\mathrm{m}} + t_{\mathrm{adh}}\frac{\partial t^{\mathrm{m}}}{\partial \tilde{u}^{\mathrm{m}}}}{H^{\mathrm{m}}\frac{\partial t^{\mathrm{m}}}{\partial \tilde{u}^{\mathrm{m}}}} \tag{33}$$

In contrast to the case of cohesive homogenisation, this expression depends on the micro model modulus of stiffness H^{m} and interface thickness t_{adh}. Since the derivative of the microscopic traction to the microscopic jump generally attains negative values, there exists a micro model size t_{adh} such that the numerator in equation (33) equals zero. The numerical difficulties encountered in this case are closely related to the phenomenon of snap back in the microscale response.

4.3.2. Case II When the adhesive interface is considerably larger than its microstructure, and in addition, the geometry in the thickness direction can be considered to be periodic, the cohesive behaviour of the interface can be described using the microscale model used for the cohesive interfaces. In contrast to the previous case, an intuitive relation between the macroscopic crack opening $\tilde{\mathbf{u}}^{\mathrm{M}}$ and microscale displacement $\mathbf{u}_{\mathrm{II}}^{\mathrm{m}}$ is missing. The homogenisation scheme is therefore derived similarly to that for of cohesive failure.

Using the definition for the macroscopic traction introduced in equation (11), the Hill-Mandel energy condition is given by

$$\frac{(w^{\mathrm{m}} - t_{\mathrm{adh}})}{w^{\mathrm{m}}}\boldsymbol{\sigma}^{\mathrm{M}} : \delta\boldsymbol{\varepsilon}^{\mathrm{M}} + \frac{1}{w^{\mathrm{m}}}\mathbf{t}^{\mathrm{M}} \cdot \delta\tilde{\mathbf{u}}^{\mathrm{M}} = \frac{1}{w^{\mathrm{m}}h^{\mathrm{m}}}\int_{\Gamma^{\mathrm{m}}} \mathbf{t}^{\mathrm{m}} \cdot \delta\mathbf{u}^{\mathrm{m}}\mathrm{d}\Gamma^{\mathrm{m}} \tag{34}$$

Using the microscale boundary conditions, this expression can be rewritten to yield

$$\mathbf{u}_{\mathrm{II}}^{\mathrm{m}} = (w^{\mathrm{m}} - t_{\mathrm{adh}})\mathbf{C}_0 \cdot \mathbf{t}^{\mathrm{M}} + \tilde{\mathbf{u}}^{\mathrm{M}} \tag{35}$$

Comparison of this expression with equation (19) shows that the homogenisation procedure for this type of adhesive failure corresponds to that of the cohesive case with the compliance scaled according to the thickness of the interface. In other words, for a thicker interface, the elastic contribution to the opening increases. As in the previously discussed case, the compatibility displacement $\mathring{\mathbf{u}}^{\mathrm{M}}$ is equal to zero due to the initial presence of the adhesive interface.

All derivations considered in the previous section apply to this case as well, and result in the system of nonlinear equations

$$\begin{pmatrix} \mathbf{f}_{\mathrm{int}}^{\mathrm{m}} - h^{\mathrm{m}}\mathbf{M}\mathbf{t}^{\mathrm{M}} \\ \mathbf{M}^{\mathrm{T}}\mathbf{a}^{\mathrm{m}} - (w^{\mathrm{m}} - t_{\mathrm{adh}})\mathbf{C}_0\mathbf{t}^{\mathrm{M}} \end{pmatrix} = \begin{pmatrix} \mathbf{0} \\ \tilde{\mathbf{u}} \end{pmatrix} \tag{36}$$

As in the case discussed above, the determinant of the matrix $\mathbf{S}$ depends on the interface thickness and interface compliance, as well as on the micro model width according to

$$D = \frac{h^{\mathrm{m}}}{K^{\mathrm{m}}} - (w^{\mathrm{m}} - t_{\mathrm{adh}})C_0 = \frac{\frac{\mathrm{d}t^{\mathrm{m}}}{\mathrm{d}\tilde{u}^{\mathrm{m}}}\big|_{\tilde{u}^{\mathrm{m}}=0} - \frac{\mathrm{d}t^{\mathrm{m}}}{\mathrm{d}\tilde{u}^{\mathrm{m}}}\left(1 - \frac{t_{\mathrm{adh}}}{w^{\mathrm{m}}} - t_{\mathrm{adh}}[H^{\mathrm{m}}]^{-1}\,\frac{\mathrm{d}t^{\mathrm{m}}}{\mathrm{d}\tilde{u}^{\mathrm{m}}}\big|_{\tilde{u}^{\mathrm{m}}=0}\right)}{\frac{\mathrm{d}t^{\mathrm{m}}}{\mathrm{d}\tilde{u}^{\mathrm{m}}}\,\frac{\mathrm{d}t^{\mathrm{m}}}{\mathrm{d}\tilde{u}^{\mathrm{m}}}\big|_{\tilde{u}^{\mathrm{m}}=0}} \tag{37}$$

This expression resembles the expression in equation (33) in the case that the micro model width equals the interface thickness. For the periodicity assumption to hold, the micro model width must be significantly smaller than the interface thickness, $w^{\mathrm{m}} \ll t_{\mathrm{adh}}$. Although the snap back problems then still can occur, choosing the micro model thickness significantly smaller than the interface thickness is beneficial from a computational effort point of view.

5. ALGORITHMIC ASPECTS

Robust and efficient implementation of the presented multiscale framework requires consideration of some algorithmic aspects. The numerical treatment of macroscale crack nucleation and step size selection for the macroscopic solution control is primarily important for robustness. The storage requirements for the micro models significantly influence the computational effort of the proposed method.

5.1. Macroscale crack nucleation

When an interface is inserted in the macro model at a nonzero stress state, as is generally the case for partition of unity based cohesive models, the microscale model needs to be activated with a nonzero initial state. This initial state is obtained by solving the microscale model for the traction obtained from the macroscale violation criterion, thereby satisfying traction-continuitiy conditions [23]. Although, in principle, this procedure is straightforward, some numerical difficulties have been identified.

In general, loading the microscale model up to the required traction level in a single step leads to divergence of the microscale Newton-Raphson solution procedure. The remedy for this problem is to simply subdivide the initial loading in several smaller loading steps. The required number of substeps strongly depends on the microscale model. For the numerical simulations considered in section 6, using 20 load steps was found to be sufficient.

Another problem occurs when the traction from a violation on the macroscale is larger than the ultimate load of the microscale model. Obviously, in this case no converged solution will be found for the microscale model. To circumvent this problem, interfaces are inserted at a traction violation which is slightly smaller than the ultimate load of the microscale model. A side effect of this remedy is that the cohesive zone in the macroscale simulation will run slightly behind the tip of the cohesive zone. The consequence for the response can be studied by considering the sensitivity of the macroscale solution to the violation traction.

Numerical problems are also encountered when a cohesive zone is extended before any microscale nonlinear behaviour has occurred. As outlined in section 4.2, this will create a singular consistent tangent matrix for the macro model. Generally, the macroscale solver will then diverge. Circumvention is possible by verifying the occurrence of nonlinear behaviour on the microscale prior to the insertion of a cohesive segment.

5.2. Macroscale solution control

The type of solution control used on the macroscale is, in principle, independent of the homogenisation scheme. Since softening mechanisms are studied, generally a peak load is observed. For this reason, force-controlled simulations are not capable of tracing the complete equilibrium path. Displacement controlled simulations can be used to determine the peak load, but fail to capture snapback behaviour. For generality, a dissipation-based arc-length control [24] has been used in this contribution.

In a monoscale simulation, the size of the energy dissipation increments is selected such that the macroscale Newton-Raphson procedure converges (typically in a few iterations). In the multiscale simulation considered here, the step size must in addition be so small that all microscale finite element models converge. Although a subdivision of the microscale loading steps as used for the micro model initialisation is possible in this case, the micro model convergence generally constrains the macroscale step size. For the simulation considered in section 6, the macroscale step size is adjusted if one or more micro models fail to converge within 10 substeps.

5.3. Microscale storage requirements

As in monoscale simulations, iterative determination of the microscale equilibrium path requires the storage of the microscale information. This information typically consists of: (i) the previously converged micro model state, (ii) the history parameters of the microscale constitutive laws, which include information on the microscale crack paths. Since these data need to be stored for all micro models, the storage requirements of the homogenisation framework can be significant. It is emphasised that the number of micro models required for the simulation of macroscale cracks is usually limited. The number of models can be reduced further by removing micro models that have fully lost their strength.

It is important to note that the previously converged state of the micro models is only updated after convergence of a macroscale simulation. In order to correctly represent the macroscale loading conditions, the state of the micro models is reset to their previously converged values before each macroscale Newton-Raphson iteration.

6. NUMERICAL SIMULATIONS

The homogenisation schemes for adhesive and cohesive failure are tested using various numerical simulations. In the first simulation, the schemes are used to derive mode I traction-opening relations for a micro model with a periodic microstructure. The influence of the micro model dimensions on the homogenised results studied. In the second simulation the homogenisation scheme for cohesive failure is used to simulate the failure process of a concrete single edge notched beam. In the third example, the homogenisation schemes for adhesive failure are tested for the delamination of a fibre-epoxy composite.

6.1. Influence of micro model dimensions

An important aspect in multiscale analyses is the existence of a representative volume element (RVE). Upon increasing the dimensions of a micro model, the homogenised behaviour of the

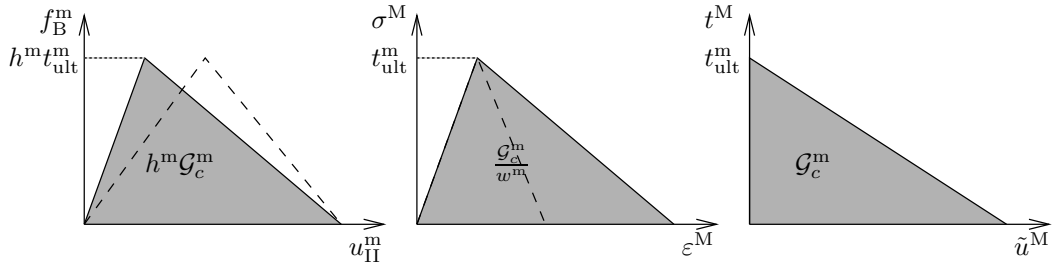

Figure 7. Response of the one-dimensional micro model in Figure 5 (left) and homogenisation results using bulk homogenisation (centre) and the cohesive homogenisation procedure introduced in section 4.2 (right). The dashed lines indicate the results for a micro model with doubled width.

model should converge. For the bulk homogenisation scheme introduced in section 4.1 the existence of an RVE has already been demonstrated and has been discussed by various authors, e.g. [25, 26]. The RVE existence for the bulk homogenisation procedure applied to softening materials was elaborately studied in Ref. [13], where it is rightfully concluded that an RVE cannot be found in that case. Here we study the influence of the micro model dimensions on the homogenisation results obtained using the proposed multiscale techniques for adhesive and cohesive failure. As we stated before, the introduced averaging procedures should be interpreted as homogenisation applied along the cracks. For that reason, using the RVE concept in its classical sense in debatable. Nevertheless, we can study the effects of the micro model dimensions on the obtained traction-opening relations. We will first do this by consideration of a simple one-dimensional problem, for which we will outline the differences in assumptions and results between the homogenisation procedures introduced in this work and the results obtained in Ref. [13]. We will then further illustrate our conclusions on the representativeness of the micro model by means of a numerical simulation.

6.1.1. One-dimensional example Consider the one-dimensional micro model introduced in Figure 5. We assume a linearly decaying initially rigid traction-opening relation for the microscale crack, with fracture strength $t_{\mathrm{ult}}^{\mathrm{m}}$ and fracture toughness $\mathcal{G}_c^{\mathrm{m}}$. The response of the micro model is shown in Figure 7 (left). As indicated in the figure, the ultimate load equals $h^{\mathrm{m}}t_{\mathrm{ult}}^{\mathrm{m}}$ and the total dissipated energy is equal to $h^{\mathrm{m}}\mathcal{G}_c^{\mathrm{m}}$. Moreover, the elastic slope is equal to $(h^{\mathrm{m}}/w^{\mathrm{m}})H^{\mathrm{m}}$ and the ultimate displacement is $2\mathcal{G}_c^{\mathrm{m}}/t_{\mathrm{ult}}^{\mathrm{m}}$. From this is is apparent that the ultimate load, the dissipated energy and elastic slope are proportional to the height of the specimen. The ultimate displacement is independent of the micro model height. The elastic slope is inversely proportional to the width of the specimen, whereas the ultimate load, ultimate displacement and dissipated energy are independent of the width.

The result of the homogenisation approach adopted in Ref. [13] to determine the stress-strain diagram is shown in Figure 7 (centre). In this homogenisation procedure, the macroscopic strain is defined as $\varepsilon^{\mathrm{M}} = u_{\mathrm{II}}^{\mathrm{m}}/w^{\mathrm{m}}$ and the macroscopic stress as $\sigma^{\mathrm{M}} = f_{\mathrm{B}}^{\mathrm{m}}/h^{\mathrm{m}}$. As indicated in Figure 7, the ultimate stress is then equal to the microscale fracture strength, and the macroscale fracture toughness is inversely proportional to the width of the micro model as $\mathcal{G}_c^{\mathrm{m}}/w^{\mathrm{m}}$. In addition, the elastic slope is equal to H^{m} and the ultimate strain is equal to $2\mathcal{G}_c^{\mathrm{m}}/(w^{\mathrm{m}}t_{\mathrm{ult}}^{\mathrm{m}})$. The independence of the elastic slope and the inverse proportionality of the dissipated energy with respect to the micro model width were also observed in Ref. [13]. From these results it is

concluded that a representative volume element can be found in the elastic regime, but not in the softening regime. In fact, increasing the width of the micro model makes the homogenised stress-strain diagram more brittle.

The homogenised traction-opening relation obtained using the multiscale scheme discussed in section 4.2 is also shown in Figure 7 (right). We will restrict the discussion here to the cohesive multiscale scheme, but similar observations can be made for the adhesive multiscale methods. The effects of the micro model dimensions on the homogenised traction-opening laws in the adhesive case will be discussed in section 6.1.2. It is assumed that the macroscopic discontinuity is inserted at the fracture strength of the micro model. Note that for the simplified model, the compatibility displacement $\mathring{u}^{\mathrm{M}}$ is equal to zero since the microscopic response prior to crack insertion is linear. Using equation (11) and (19), the macroscopic traction and crack opening are then obtained as

$$t^{\mathrm{M}} = \frac{f_{\mathrm{B}}^{\mathrm{m}}}{h^{\mathrm{m}}} \qquad \text{and} \qquad \tilde{u}^{\mathrm{M}} = u_{\mathrm{II}}^{\mathrm{m}} - \frac{w^{\mathrm{m}}}{h^{\mathrm{m}}} \frac{f_{\mathrm{B}}^{\mathrm{m}}}{H^{\mathrm{m}}} \tag{38}$$

From the first expressions it is directly observed that the homogenised fracture strength is equal to the microscale fracture strength. From the second expression it can be seen that the ultimate crack opening (at $f_{\mathrm{B}}^{\mathrm{m}} = 0$) is equal to the ultimate displacement of the micro model, which reflects the fact that in that case the elastic displacement of the micro model equals zero. The macroscopic fracture energy as obtained using the proposed homogenisation scheme is equal to the microscopic fracture energy. Hence, in contrast to the bulk homogenisation scheme the macroscale fracture toughness is independent of the width of the micro model.

The analysis of the one-dimensional example illustrates the differences between the bulk homogenisation approach and the multiscale approach presented in this work. It shows that the inverse proportionality of the homogenised fracture toughness as obtained when applying bulk homogenisation, is eliminated when the cohesive homogenisation scheme is used. However, it needs to be remarked that the objectivity of the micro model width is compromised when some microscale dissipation has occurred before the insertion of a macroscale cohesive segment (i.e. when $\mathring{\mathbf{u}}^{\mathrm{m}} \neq \mathbf{0}$). In that case, the amount of dissipation before insertion can depend on the width of the specimen, decreasing the homogenised fracture toughness. An important assumption for the validity of the proposed multiscale schemes is therefore that the microscale dissipation prior to macroscopic crack insertion is very small compared to the total dissipation of the micro model. Under that assumption, increasing the width of the micro model will hardly affect the homogenised traction-opening law. In particular, doubling the width of the micro model will not decrease the fracture toughness by a factor of two (as in the case of bulk homogenisation). This will be confirmed by the numerical simulations considered in the next section.

6.1.2. Numerical example Consider a micro model of $0.5 \times 0.5\,\mathrm{mm}^2$ with a centred circular inclusion of diameter 0.25 mm, referred to as "Micro model 1" in Figure 8. A plane stress state is assumed for the micro model. The material of the inclusion is modelled using a linear elastic isotropic law with a modulus of elasticity of 50 GPa and a Poisson ratio of 0.25. The surrounding material is modelled with a linear elastic isotropic law with the same Poisson ratio and a modulus of elasticity of 5 GPa. Cohesive fracture of the surrounding material is modelled using the initially rigid mixed-mode cohesive law proposed by Wells and Sluys [15], with a fracture strength of 5 MPa and a fracture toughness of 0.01 N/mm. The damage in shear direction is

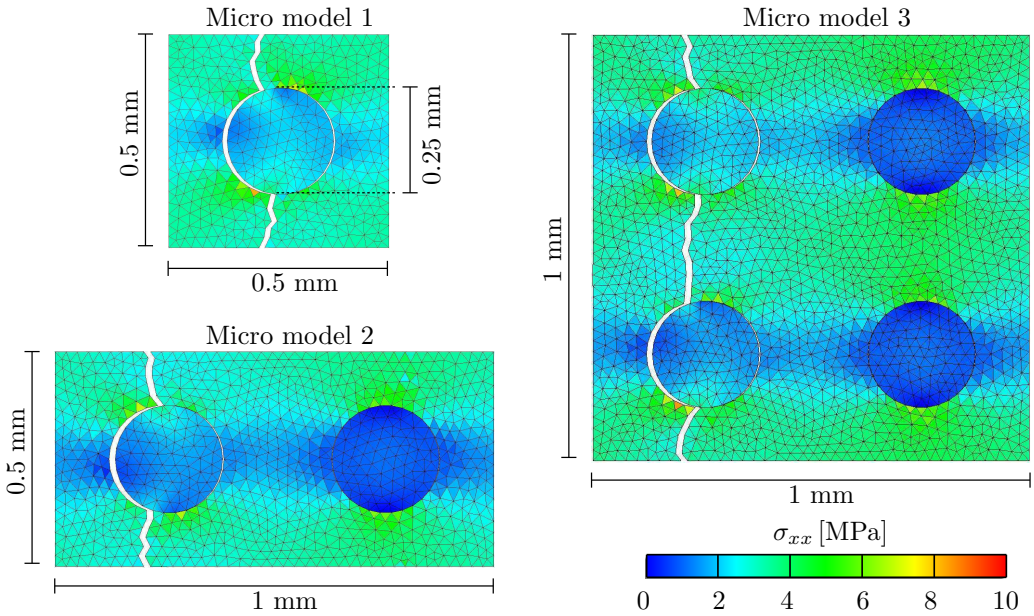

Figure 8. Microstructural models of different dimensions with the same periodic microstructure. The displacements are magnified by a factor of 10. The contour plots show the Cauchy stress in the horizontal direction.

taken the same as in the normal direction, and the initial stiffness in shear direction is taken as 1 MPa/mm. The adhesive interface between the inclusion and the surrounding material is modelled using the initially elastic traction-opening relation proposed by Xu and Needleman [27]. The fracture toughnesses in normal (mode I) and shear (mode II) directions are assumed to be equal and the opening in normal direction after complete shear failure is assumed to be equal to zero in the case of zero normal traction. The fracture strength and fracture toughness for this material interface are taken as 2.5 MPa and 0.005 N/mm, respectively. In addition, a penetration stiffness of $1 \cdot 10^8$ MPa/mm is used for both traction-opening laws.

The response of "Micro model 1" measured as the force over the right edge $\mathbf{f}_{\mathrm{B}}^{\mathrm{m}}$ versus the displacement of the bottom-right control node $\mathbf{u}_{\mathrm{II}}^{\mathrm{m}}$ is shown in Figure 9 for the case of mode I loading. When loading the micro model, the adhesive interface starts to damage, after which cracks nucleate into the surrounding material. While the cracks propagate, the micro model degradates and finally loses all strength. As can be seen in Figure 8, the crack path is forced to be periodic. The experiment is repeated for two other micro models with different dimensions as shown in Figure 8. As observed from Figure 9, the response of the other micro models differs significantly from that of "Micro model 1". Increasing the width of the micro model ("Micro model 2") results in larger displacements, since the effective flexibility of the micro model is increased. Increasing the height of the micro model ("Micro model 3") clearly increases the load-bearing capacity of the micro model.

The homogenisation scheme for cohesive failure is applied to the three micro model simulations discussed above. The micro models are assumed to be activated at a normal traction of 3.7 MPa, which is slightly smaller than the homogenised fracture strength. The

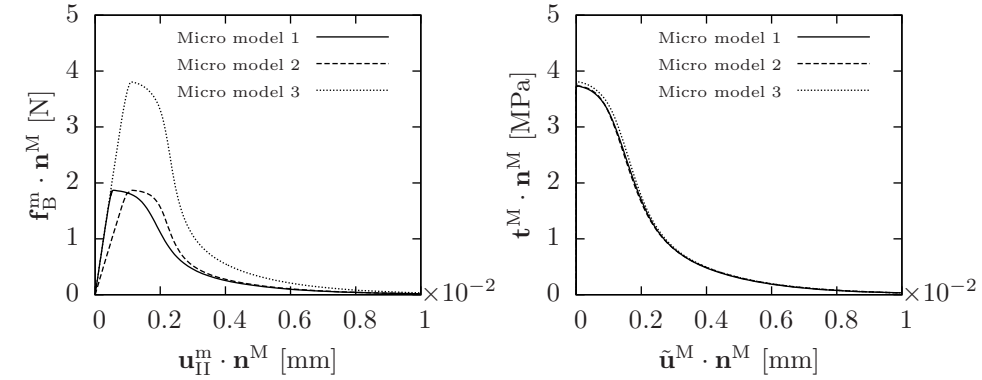

Figure 9. Microscale force-displacement diagrams (left) and corresponding homogenised traction-opening relations (right) for cohesive failure.

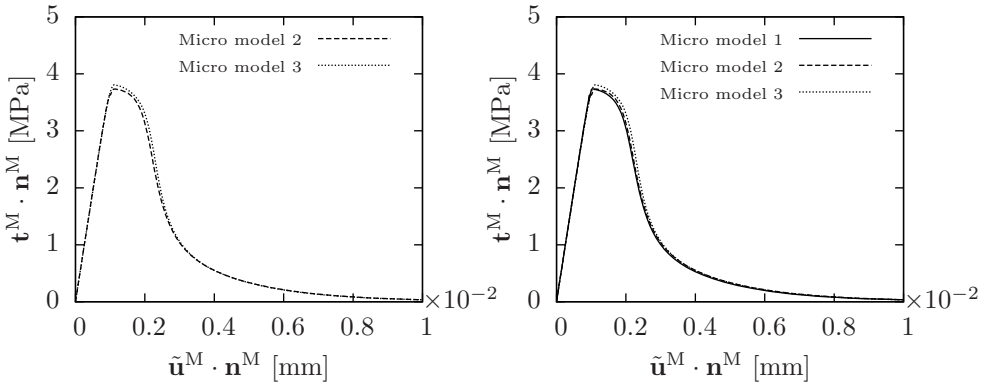

Figure 10. Homogenised traction-opening laws for adhesive failure of an interface with a thickness of $t_{\mathrm{adh}} = 1$ mm. Note that since the width of micro model 1 does not match the thickness of the interface, it cannot be used for the Case I homogenisation scheme (left). It can, however, be used for the Case II scheme (right).

homogenised traction-opening laws in normal direction for the three micro models are shown in Figure 9. As can be seen, the results for the various micro models coincide. This confirms that the homogenised traction-opening relation is practically independent of the dimensions of the micro model when the amount of microscale energy dissipation prior to macroscopic crack insertion is very small compared to the total dissipation. When the considered microstructure is random, the homogenised tracton-opening laws will not coincide for all considered micro model dimensions. However, upon increase of the size of the micro model, the spread in the results should diminish. A detailed study of the statistical convergence of the proposed homogenisation schemes, as performed in Ref. [13] for bulk homogenisation, is a topic of further study.

The dependence of the homogenised adhesive traction-opening laws on the micro model dimensions is studied by assuming an interface thickness t_{adh} of 1 mm. For the adhesive homogenisation scheme in which the micro model width coincides with the thickness of the

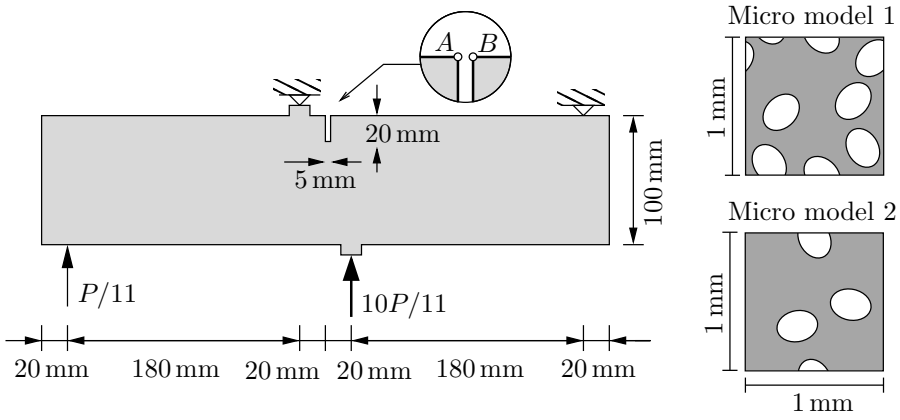

Figure 11. Schematic representation of the single edge notched (SEN) beam (left), with two geometrically periodic micro models. The depth of the beam is 100 mm.

interface (Case I), only "Micro mode 2" and "Micro model 3" can be used. The homogenised traction-opening laws are shown in Figure 10. Since the homogenised behaviour is independent of the micro model height, it can be regarded as an RVE for the Case I homogenisation scheme. For the Case II scheme, in which the micro model width is independent of the interface thickness, all three micro models can be used. The homogenisation results are shown in Figure 10. The results for "Micro model 2" and "Micro model 3" obviously resemble the Case I results. In this case, however, the homogenised traction-opening law found for "Micro model 1" also matches the same result. As for the cohesive multiscale scheme, the homogenised properties are observed to be practically independent of the micro model dimensions.

6.2. Cohesive failure

The homogenisation law for cohesive failure is demonstrated on the basis of the single edge notched (SEN) beam, as shown in Figure 11. The beam is made of a cementitious material, of which the microstructure is composed of aggregates and cement. A plane stress state is assumed for both the macroscale and microscale model. Two different microstructures are studied, as also shown in Figure 11. Both micro models have a size of $1 \times 1\,\mathrm{mm}^2$. The first micro model contains 6 elliptic stones with a minor and major diameter of $0.25/\sqrt{1.25}\,\mathrm{mm}$ and $0.25 \cdot \sqrt{1.25}\,\mathrm{mm}$, respectively (consequentially the ellipticity equals 1.25). The second micro model contains half the volume fraction of similar stones. The material parameters for the microstructure resemble those used by Tijssens et. al. [28]. Both the cement and stones are modelled using a linear elastic isotropic constitutive law. The modulus of elasticity and Poisson ratio of the cement are equal to 20 GPa and 0.2, respectively. For the stones these parameters are taken as 55 GPa and 0.2. Cohesive cracks are permitted in the cement, which has a fracture strength of 5 MPa and a fracture toughness of 0.019 N/mm. The material interfaces between the stones and cement have a fracture strength of 2.1 MPa and fracture toughness of 0.003 N/mm. The same constitutive laws are used as in the previous section, for both the adhesive and cohesive interfaces. Note that the considered micro models are probably not large enough to be considered as statistical RVEs. The models are, however, suitable to demonstrate how the

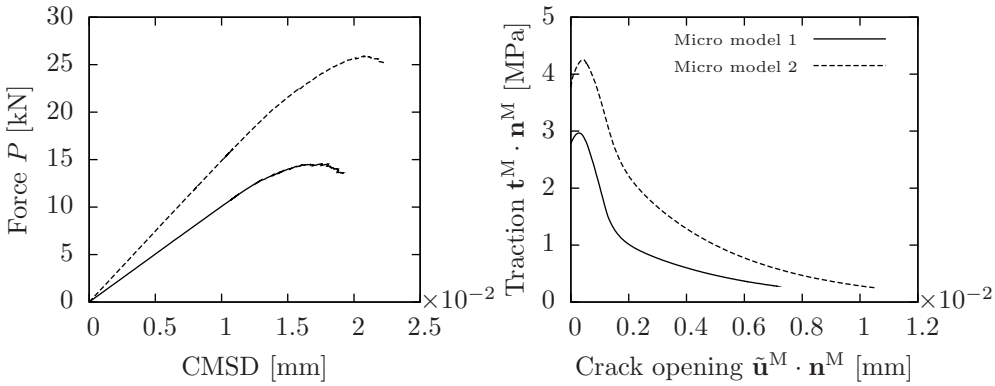

Figure 12. Load P versus the crack-mouth sliding displacement (CMSD) for the SEN-beam (left) and a typical macroscopic normal traction versus normal crack opening curve (right).

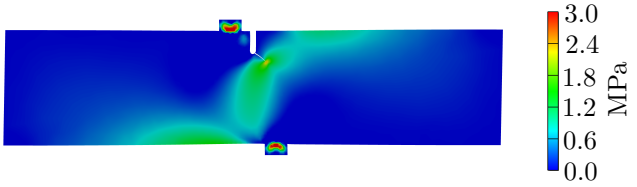

Figure 13. Maximum principal stress contour plot for the SEN-beam.

homogenisation framework can be used to gain insight in the influence of the microstructure on the macroscale behaviour.

On the macroscale, failure of the SEN-beam is modelled using a partition of unity-based cohesive zone method [16, 15, 29]. In this method, piecewise continuous finite element shape functions are enhanced with Heaviside functions, in order to mimic cohesive cracks by jumps in the displacement field. Crack nucleation is based on the principal stress values in the macroscale integration points. Crack propagation is based on the principal components of an averaged stress tensor in the crack tip [30, 31]. Upon increasing the load P, a macroscopic crack will nucleate at the tip of the notch. Upon further increase of the loading, the crack will propagate, until the ultimate load is reached.

The response of the SEN-beam is measured in terms of the load P versus the crack mouth sliding displacement (CMSD), which is defined as the difference in vertical displacement of the points A and B indicated in Figure 11. The response with "Micro model 1" is shown in Figure 12. The ultimate load of the specimen is observed to be equal to 14.5 N. The observed wiggles are caused by the nonlocal estimation of the crack-tip stress and can be further reduced by mesh refinement. However, since the number of cohesive integration points increases by refining the mesh, this would have significantly increased the required computational effort. The macroscopic crack path and contour plot of the maximum principal stress are shown in Figure 13 and a traction-opening law realised for one of the macroscopic integration points is shown in Figure 12. The corresponding fractured micro model is presented in Figure 14.

In Figure 12, the response of the SEN-beam with "Micro model 2" is also incorporated.

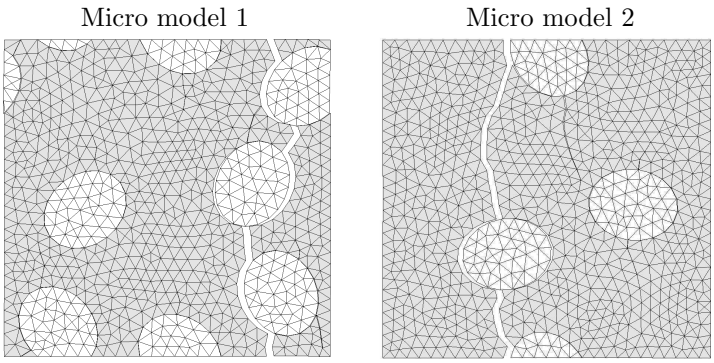

Figure 14. Fractured micro models used for the cohesive homogenisation scheme. Deformations are scaled by a factor of 20.

As can be seen, a significantly higher ultimate load of 25.9 N is observed. A typical traction-opening law, as shown in Figure 12, reveals that this increase is caused by the fact that the fracture strength of the composite with a smaller volume fraction of stones is considerably larger. The larger fracture toughness is also reflected in the macroscale force-displacement curve. Comparison of two fractured micro models gives a microstructural explanation for the observed differences. As can be seen in the case of the smaller fibre volume fraction, a significantly larger part of the crack path runs through the epoxy. Since both the fracture strength and fracture toughness of the epoxy are considerably larger than those of the fibre-epoxy interface, the homogenised fracture strength and fracture toughness are also significantly larger. Again it is emphasised that for a quantitive comparison of the two cases the micro model size needs to be large enough to ensure it to be a statistical representative volume element.

6.3. Adhesive failure

The peel test, schematically shown in Figure 15, is used to demonstrate the homogenisation framework for adhesive failure. The numerical experiment represents the failure of a fibre-epoxy composite material as presented in [32]. Two layers of horizontally aligned (in the x_1^{M}-direction) fibres are connected by an 80 micron thick interfacial layer (dashed line) of fibres oriented in the in-plane direction. A plane stress state is assumed for the specimen with a depth of 20 mm. The layers of horizontally aligned fibres are modelled using an orthotropic Hookean law with elastic moduli $E_{11} = 120\,\mathrm{GPa}$, $E_{22} = 10.5\,\mathrm{GPa}$ and $G_{12} = 5.25\,\mathrm{GPa}$ and Poisson ratio $\nu_{12} = 0.3$. To mimic the failure process of the composite specimen, microscale models are used to describe the constitutive behaviour of the predefined interface indicated in Figure 15. On this microscale, the material is composed of a mix of epoxy with 5 μm radius circular fibres. Both the fibres and epoxy are modelled using a isotropic Hookean law. The modulus of elasticity and Poisson ratio of the epoxy are taken as 4.3 GPa and 0.34, respectively. For the fibres a Young's modulus of 225 GPa and Poisson ratio 0.2 are used. The cohesive failure of the epoxy material is governed by the cohesive law discussed in section 6.1 with a fracture strength of 15 MPa and fracture toughness of 0.2 N/mm. For the adhesive failure of the fibre-epoxy interfaces, a bilinear traction-opening law is considered. The fracture toughness is taken equal to that of the epoxy material and the fracture strength is taken as 20 MPa. The initial

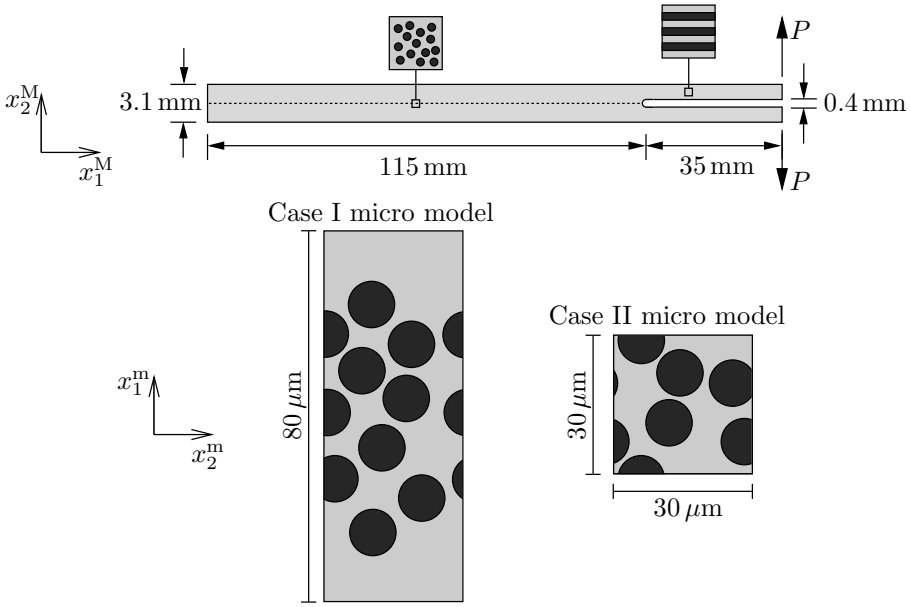

Figure 15. Schematic representation of the fibre-epoxy peel specimen with a depth of 20 mm. The fibre-direction in the predefined interface layer (dashed line) is orthogonal to that in the adjacent layers. Note that the width of the Case I micro model corresponds with the the height of the macroscopic interface.

stiffness, which is an independent material parameter for this constitutive model, is taken as $2 \cdot 10^6$ MPa/mm.

Since a predefined interface is considered in this case, the macroscale problem is modelled using an interface elements formulation. Although not strictly necessary for the considered simulation, finite strain kinematics are used on the macroscale. A total Lagrangian formulation [33] is employed to model the geometric nonlineartities. Due to the symmetry of the problem, the rotation of the predefined interface remains equal to zero.

Homogenisation using the Case II adhesive homogenisation scheme is performed using a $30 \times 30\,\mu\mathrm{m}^2$ micro model as shown in Figure 15. Note that due to the small separation in lengths of the interface thickness and micro model size, the periodicity assumption is violated. The presented simulation, however, remains applicable for illustration purposes. The force-displacement curve for the peel test is shown in Figure 16, where the crack mouth opening displacement (CMOD) is used as a displacement measure. From the force-displacement diagram an ultimate load of 50.3 N is observed. A typical traction-opening law which is implicitly provided by the homogenisation scheme is also shown in this figure. Note that the fracture strength and fracture toughness roughly match the mode I parameters reported in [32]. A typical fractured micro model is shown in Figure 17. We remind that generally the homogenised traction-opening law and cracked micro model are different for each macroscopic integration point.

In realistic fibre-epoxy layers an epoxy rich region is often observed at the edges of the

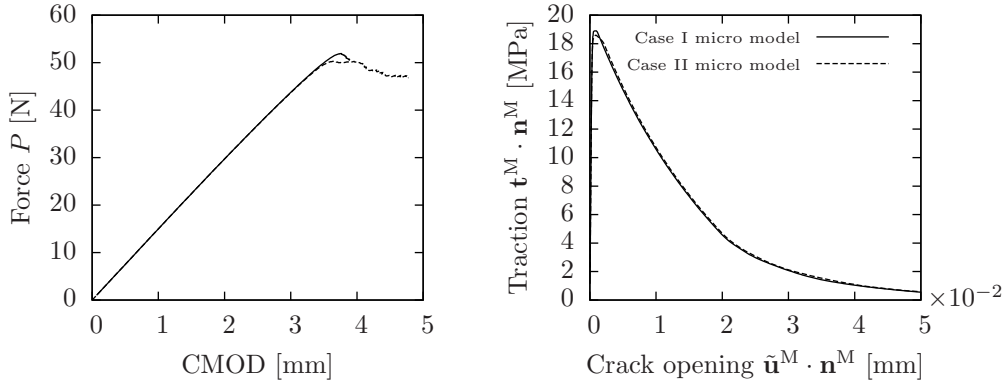

Figure 16. Load P versus the crack-mouth opening displacement (CMOD) for the peel test (left) and a typical macroscopic normal traction versus normal crack opening curve (right).

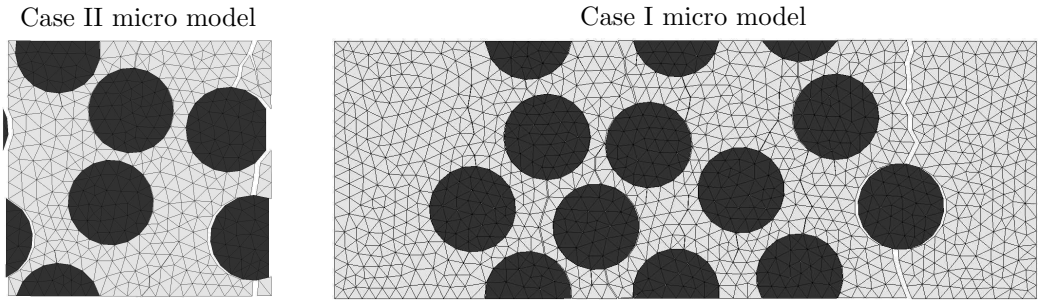

Figure 17. Fractured micro models used for the adhesive homogenisation scheme.

interface [34]. Obviously, the periodicity assumption cannot be made in such a case and hence the Case II homogenisation scheme cannot realistically mimic the fracture behaviour of the interface. In the Case I homogenisation scheme this can be done since no assumptions on the periodicity in the x_1^{m}-direction are made. An $80 \times 30\,\mu\mathrm{m}^2$ micro model is used in that case (see Figure 15), where it is assumed that no fibres are present within $10\,\mu$m of the physical edges of the interface. The force-displacement diagram and a typical corresponding characteristic traction-opening relation are shown in Figure 16. The ultimate load predicted using the Case I homogenisation scheme is 51.9 N, which closely resembles the result obtained using the Case II scheme (50.2 N). The similarity can also be observed from the traction-opening laws, as shown in Figure 16. Considering some of the cracked micro models, as shown in Figure 17, reveals the micromechanical reason for these similarities. In the Case II homogenisation scheme, cracks run both through the epoxy and along the fibre edges. Although cracks have the tendency to run through the epoxy rich regions in the Case I homogenisation scheme, the evolved cracks continue to run through both the cohesive and adhesive interfaces. As a result no fundamental difference in fracture behaviour is observed for the considered micro scale models. By changing the material parameters, it should be possible to get the crack to run completely through the epoxy rich region in the Case I scheme. In that case, the use of

the Case II homogenisation scheme will not realistically mimic the microscale fracture process. In addition it is mentioned that the micro model dimensions are not large enough to regard them as statistical representative volume elements. Nonetheless, they give a good insight in the usefulness of the homogenisation schemes.

7. CONCLUSIONS

A computational homogenisation framework to model cohesive and adhesive failure in materials with complex microstructures has been proposed. Consistent with the employed macroscale discrete fracture models, computational homogenisation (an FE^2-approach) is only adopted in the integration points on the crack surface. Numerical homogenisation is used to derive effective material tangents for the macroscale bulk constitutive law. As a consequence of the adopted multiscale strategy, the number of microscale FE-models to be solved equals the number of integration points on the fracture surfaces. From a computational effort point of view this makes the proposed framework attractive compared to FE^2-models in which microscale models are solved in all integration points.

Using the Hill energy principle, homogenisation relations are derived for cohesive and adhesive failure. In the former case, the resulting traction-opening law is initially rigid, whereas in the latter case an initially elastic law is obtained. The occurrence of microscale snapback, which generally causes robustness problems, is dealt with by using the homogenisation relations as path-following constraints.

The dependence of the homogenised constitutive laws on the micro model size is studied using a one-dimensional example. From this analysis it is observed that for the proposed homogenisation method an objective micro model size can be selected. These results are confirmed by the numerical simulation of a micro model with a periodic microstructure. The investigation of the representativeness of micro models with a random microstructure is a topic of further study. Numerical simulations using a partition of unity-based crack model and interface elements-based crack model on the macroscale demonstrate the applicability of the proposed homogenisation schemes for cohesive and adhesive failure.

ACKNOWLEDGEMENTS

The research leading to these results has received funding from the European Community's Seventh Framework Programme FP7/2007-2013 under grant agreement n°213371.

REFERENCES

1. W. Voigt. Über die beziehung zwischen den beiden elasticitätsconstanten isotroper körper. *Annalen der Physik*, 274:573–587, 1889.
2. A. Reuss. Berechnung der fließgrenze von mischkristallen auf grund der plastizitätsbedingung für einkristalle. *Zeitschrift für Angewandte Mathematik und Mechanik*, 9:49–58, 1929.
3. J. D. Eshelby. The determination of the elastic field of an ellipsoidal inclusion, and related problems. *Proceedings of the Royal Society of London. Series A, Mathematical and Physical Sciences*, 241:376–396, 1957.

4. P. M. Suquet. Local and global aspects in the mathematical theory of plasticity. In A. Sawczuk and G. Bianchi, editors, *Plasticity today: modelling, methods and applications*, pages 279–310, London, 1985. Elsevier.
5. F. Feyel. Multiscale FE^2 elastoviscoplastic analysis of composite structures. *Computational Materials Science*, 16(1–4):344–354, 1999.
6. V. G. Kouznetsova, M. G. D. Geers, and W. A. M. Brekelmans. Multi-scale constitutive modelling of heterogeneous materials with a gradient-enhanced computational homogenization scheme. *International Journal for Numerical Methods in Engineering*, 54(8):1235–1260, 2002.
7. F. Feyel. A multilevel finite element method (FE^2) to describe the response of highly non-linear structures using generalized continua. *Computer Methods in Applied Mechanics and Engineering*, 192(28-30):3233–3244, 2003.
8. K. Matouš, M. G. Kulkarni, and P. H. Geubelle. Multiscale cohesive failure modeling of heterogeneous adhesives. *Journal of Mechanics and Physics of Solids*, 56(4):1511–1533, 2008.
9. C. B. Hirschberger, N. Sukumar, and P. Steinmann. Computational homogenization of material layers with micromorphic mesostructure. *Philosophical Magazine*, 88(30):3603–3631, 2008.
10. T. Belytschko, S. Loehnert, and J. H. Song. Multiscale aggregating discontinuities: a method for circumventing loss of material stability. *International Journal for Numerical Methods in Engineering*, 73(6):869–894, 2008.
11. T. Hettich, A. Hund, and E. Ramm. Modeling of failure in composites by x-fem and level sets within a multiscale framework. *Computer Methods in Applied Mechanics and Engineering*, 197(5):414–424, 2008.
12. C. V. Verhoosel, J. J. C. Remmers, and M. A. Gutiérrez. A partition of unity-based multiscale approach for modelling failure in piezoelectric components. *International Journal for Numerical Methods in Engineering*, 2009. Accepted.
13. I. M. Gitman, H. Askes, and L. J. Sluys. Representative volume: Existence and size determination. *Engineering Fracture Mechanics*, 74(16):2518–2534, 2007.
14. G. T. Camacho and M. Ortiz. Computational modelling of impact damage in brittle materials. *International Journal of Solids and Structures*, 33(20–22):2899–2938, 1996.
15. G. N. Wells and L. J. Sluys. A new method for modelling cohesive cracks using finite elements. *International Journal for Numerical Methods in Engineering*, 50(12):2667–2682, 2001.
16. N. Moës and T. Belytschko. Extended finite element method for cohesive crack growth. *Engineering Fracture Mechanics*, 69(7):813–833, 2002.
17. G. N. Wells, R. de Borst, and L. J. Sluys. A consistent geometrically non-linear approach for delamination. *International Journal for Numerical Methods in Engineering*, 54(9):1333–1355, 2002.
18. R. H. J. Peerlings, R. de Borst, W. A. M. Brekelmans, and M. G. D. Geers. Localisation issues in local and nonlocal continuum approaches to fracture. *European Journal of Mechanics - A/Solids*, 21(2):175–189, 2002.
19. R. Hill. Elastic properties of reinforced solids: some theoretical principles. *Journal of the Mechanics and Physics of Solids*, 11(5):357–372, 1963.
20. V. G. Kouznetsova, W. A. M. Brekelmans, and F. P. T. Baaijens. An approach to micro-macro modeling of heterogeneous materials. *Computational Mechanics*, 27(1):37–48, 2001.
21. M. C. Cid Alfaro, A. S. J. Suiker, C. V. Verhoosel, and R. de Borst. Computational homogenization of cracking processes in thin fibre-expoxy layers. *European Journal of Mechanics - A/Solids*, 2009. doi:10.1016/j.euromechsol.2009.09.006.
22. I. M. Gitman, H. Askes, and L. J. Sluys. Coupled-volume multi-scale modelling of quasi-brittle material. *European Journal of Mechanics - A/Solids*, 27(3):302–327, 2008.
23. K. D. Papoulia, C. H. Sam, and S. A. Vavasis. Time continuity in cohesive finite element modeling. *International Journal for Numerical Methods in Engineering*, 58(5):679–701, 2003.
24. C. V. Verhoosel, J. J. C Remmers, and M. A. Gutiérrez. A dissipation-based arc-length method for robust simulation of brittle and ductile failure. *International Journal for Numerical Methods in Engineering*, 77(9):1290–1321, 2009.
25. Kenjiro Terada, Muneo Hori, Takashi Kyoya, and Noboru Kikuchi. Simulation of the multi-scale convergence in computational homogenization approaches. *International Journal of Solids and Structures*, 37(16):2285–2311, 4 2000.
26. T. I. Zohdi. *Encyclopedia of Computational Mechanics*, volume 2: Solids and Structures, chapter Homogenization methods and multiscale modellng, pages 335–373. Wiley, Chichester, 2004.
27. X. P. Xu and A. Needleman. Void nucleation by inclusion debonding in a crystal matrix. *Modelling and Simulation in Materials Science and Engineering*, 1(2):111–132, 1993.
28. M. G. A. Tijssens, L. J. Sluys, and E. van der Giessen. Simulation of fracture of cementitious composites with explicit modeling of microstructural features. *Engineering Fracture Mechanics*, 68(11):1245–1263, 2001.
29. J. J. C. Remmers, R. de Borst, and A. Needleman. A cohesive segments method for the simulation of

crack growth. *Computational mechanics*, 31(1-2):69–77, May 2003.
30. M. Jirásek. Embedded crack models for concrete fracture. In R de Borst, N Bicanic, H Mang, and G Meschke, editors, *Proceedings of Computational Modelling of Concrete Structures*, pages 291–300, Rotterdam, 1998. Balkema.
31. M. Jirásek. Comparative study on finite elements with embedded discontinuities. *Computer Methods in Applied Mechanics and Engineering*, 188(1-3):307–330, 2000.
32. A. Turon, P. P. Camanho, J. Costa, and J. Renart. Accurate simulation of delamination growth under mixed-mode loading using cohesive elements: definition of interlaminar strengths and elastic stiffness. In press.
33. K. J. Bathe. *Finite Element Procedures*. Prentice Hall, Upper Saddle River, 1996.
34. J. J. C. Remmers and R. de Borst. Delamination buckling of fibre-metal laminates. *Composites Science and Technology*, 61(15):2207–2213, 2001.